Structure and dynamics of low Reynolds number turbulent pipe flow

By Andrew Duggleby[1,*], Kenneth S. Ball[2] and Markus Schwaenen[1]

[1]*Department of Mechanical Engineering, Texas A&M University, College Station, TX 77843, USA*
[2]*Department of Mechanical Engineering, Virginia Polytechnic Institute and State University, Blacksburg, VA 24061, USA*

Using large-scale numerical calculations, we explore the proper orthogonal decomposition of low Reynolds number turbulent pipe flow, using both the translational invariant (Fourier) method and the method of snapshots. Each method has benefits and drawbacks, making the 'best' choice dependent on the purpose of the analysis. Owing to its construction, the Fourier method includes all the flow fields that are translational invariants of the simulated flow fields. Thus, the Fourier method converges to an estimate of the dimension of the chaotic attractor in less total simulation time than the method of snapshots. The converse is that for a given simulation, the method of snapshots yields a basis set that is more optimal because it does not include all of the translational invariants that were not a part of the simulation. Using the Fourier method yields smooth structures with definable subclasses based upon Fourier wavenumber pairs, and results in a new dynamical systems insight into turbulent pipe flow. These subclasses include a set of modes that propagate with a nearly constant phase speed, act together as a wave packet and transfer energy from streamwise rolls. It is these interactions that are responsible for bursting events and Reynolds stress generation. These structures and dynamics are similar to those found in turbulent channel flow. A comparison of structures and dynamics in turbulent pipe and channel flows is reported to emphasize the similarities and differences.

Keywords: proper orthogonal decomposition; turbulence; pipe flow; structures; dynamics; channel flow

1. Introduction: structures in wall-bounded flows

One hundred and twenty-five years after Reynolds' (1883) seminal paper on transition of flow in a pipe from laminar to turbulent, turbulence remains difficult to fully understand and predict. The difficulty lies in the nonlinear dynamics inherent to the flows. These nonlinearities populate a broad range of spatial and temporal scales with sensitive dependence on initial conditions (chaos).

* Author for correspondence (aduggleby@tamu.edu).

One contribution of 10 to a Theme Issue 'Turbulence transition in pipe flow: 125th anniversary of the publication of Reynolds' paper'.

Since Reynolds' (1883) paper, many discoveries in the theoretical under-standing of turbulence have been made. Such notable theories by Taylor (1921) on turbulent transport, Keller & Friedmann (1925) on statistical moments of fluids, Prandtl (1925) and von Kármán (1930) on semi-empirical theory, Taylor (1935) on small-scale motion and Kolmogorov (1941) on the local isotropy of turbulence form the foundation of turbulence research.

Starting in the 1950s, a new approach to turbulence based upon dynamical systems pioneered by Townsend (1956), Kline *et al.* (1967), Blackwelder & Eckelmann (1979) and Robinson (1991) began. This approach focuses on characterizing the coherent structures responsible for turbulent stress, momentum and energy transport. Collectively, this line of research is largely responsible for the classification and visualization of structures, and the interpretation of motions and dynamics such as bursting events that form a foundation for the current understanding of turbulence. Despite this significant step forward, the exact nature of a coherent vortex and the criterion used to find it is still a debated subject (see Green *et al.* 2007).

Furthering this dynamical systems approach was the advancement of super-computing in the early 1990s that made accessible the use a powerful statistical analysis method for turbulence. This method, known as Karhunen–Loève or proper orthogonal decomposition (POD), decomposes a dataset into its most optimal basis functions in L_2. This method was first applied to turbulent flows by Lumley (1967) for homogeneous turbulence, and was extended to channel flow by Sirovich *et al.* (1990, 1991) and Ball *et al.* (1991). Successes with this method include Sirovich *et al.* (1991) who explained bursting and sweeping events, and Webber *et al.* (2002) who explained energy transfer between the structures. POD was recently extended to turbulent pipe flow by Duggleby *et al.* (2007b), and was used to explain drag reduction by spanwise wall oscillation in Duggleby *et al.* (2007a).

But the work of understanding turbulence is not done. As long as aircraft, cars, boats, etc. are built, turbines are used to extract energy from heat and pipes form the infrastructure of our society's transport of gas, oil and water, the need to improve the understanding of turbulent flow continues. As computational power continues to increase, so too will the usefulness of POD in turbulence analysis. This paper will review POD; discuss the two primary methods of applying POD; present the structures, dynamics and understanding uncovered in its analysis of turbulent pipe flow; and compare these structures with those found in turbulent channel flow.

2. Numerical methods

(*a*) *Direct numerical simulations*

Large-scale numerical simulations offer a unique avenue for theoretical research in turbulent flows, in that entire velocity and pressure fields may be captured at any instant in time, and as often as needed (resources permitting). The confidence in the data generated by these simulations is founded on the well-defined Navier–Stokes model for the conservation of mass and momentum for an incompressible Newtonian fluid. The model written in its non-dimensional form is

$$\partial_t \boldsymbol{U} + \boldsymbol{U} \cdot \nabla \boldsymbol{U} = -\nabla P + Re_\tau^{-1} \nabla^2 \boldsymbol{U}, \tag{2.1}$$

$$\nabla \cdot \boldsymbol{U} = 0, \tag{2.2}$$

where $\boldsymbol{U}$ is the velocity vector; Re_τ is the Reynolds number; P is the pressure; and t is the time. The wall shear velocity $U_\tau = \sqrt{\tau_w/\rho}$ and a length scale (radius R for a pipe or channel half-height $h/2$ for a channel) are used to non-dimensionalize the equation, where τ_w is the wall shear stress and ρ is the density. The Reynolds number is defined as $Re_\tau = U_\tau R/\nu$ for a pipe and $Re_\tau = U_\tau h/\nu$ for a channel, where ν is the kinematic viscosity.

The method for solving these equations for all possible temporal and spatial scales (known as direct numerical simulation or DNS) comes at a cost. The computational operations scale as Re_τ^4 and storage requirements scales as $Re_\tau^{9/4}$. Additionally, in order to make the most efficient use of computational resources and to avoid numerical errors due to discretization, high-order numerical schemes are typically used. For this work, both the turbulent pipe and channel flow data are generated by DNS using the following algorithms.

(i) *Turbulent pipe flow*

The turbulent pipe flow data are generated using a globally high-order spectral element algorithm. The flow is driven by a mean streamwise pressure gradient to obtain a Reynolds number of $Re_\tau = 150$. When non-dimensionalized with the mean velocity U_m, the Reynolds number is $Re_m = U_m D/\nu \approx 4300$. The domain length is $L = 20R = 10D$ (diameters) or $z^+ = 3000$ in wall units (distance non-dimensionalized by the length ν/U_τ), which is long enough to use periodic boundary conditions to achieve realistic turbulent inlet and outlet conditions. Data are acquired for 2100 samples every $t^+ = 8$. This corresponds to a total simulation time of $t^+ = U_\tau^2 t/\nu = 16\,800$ viscous time units, which is roughly $(tU_m/D \approx 800)$. Further details on the numerical scheme can be found in Fischer *et al.* (1988) and Tufo & Fischer (1999), as well as its specific application to pipe flow in Duggleby *et al.* (2007*b*).

(ii) *Turbulent channel flow*

For comparison of turbulent pipe flow with turbulent channel flow, two datasets are used. The first data are those analysed by Ball *et al.* (1991), and are generated by a DNS of the Navier–Stokes equations performed by L. Keefe (see Kim *et al.* (1987) for details on the numerical scheme). A spectral method (Fourier and Chebyshev series in the homogeneous and wall-normal directions) is employed for the spatial derivatives, whereas the time and nonlinear terms are discretized using semi-implicit schemes. The flow is driven by a mean streamwise pressure gradient, yielding a Reynolds number of $Re_\tau = 80$. The domain consists of $24 \times 33 \times 12$ grid points spanning $5h$, $2h$ and $5h$ in the streamwise, wall-normal and spanwise directions (x, y, z), respectively. The boundary conditions are periodic in the streamwise and spanwise directions and no slip in the wall-normal direction. Data are acquired for 500 time samples $t^+ = 8.4$ apart, corresponding to $390\,U_m/h$. The chaotic turbulent attractor is further sampled by taking advantage of the symmetries inherent to the channel geometry.

In order to visualize flow features using more recent techniques, new data are generated using a commercial finite-volume (FV) algorithm, using a domain that is twice as long ($10h$) and the same flow parameters. The grid resolution is refined to $135 \times 90 \times 134$ in the streamwise, wall-normal and spanwise directions,

respectively, to account for lower accuracy of the discretization procedure. The largest grid spacing does not exceed twice the estimated Kolmogorov microscale. Turbulence modelling is turned off, solving the Navier–Stokes equations (equations (2.1) and (2.2)) with only the molecular viscosity (no turbulent viscosity). A second-order implicit scheme is used for time advancement and a third-order monotone upstream-centred schemes for conservation laws scheme for spatial derivatives.

(*b*) *Proper orthogonal decomposition*

A very useful technique that takes advantage of the richness of data obtained through DNS of turbulence is the extraction of structures and dynamics through a POD (or Karhunen–Loève decomposition). This involves solving the Fredholm integral equation

$$\int_{\Omega} K(\ell, \ell') \boldsymbol{\Phi}(\ell') \mathrm{d}\Omega = \lambda \boldsymbol{\Phi}(\ell), \tag{2.3}$$

$$K(\ell, \ell') = \lim_{T \to \infty} \frac{1}{T} \int_{0}^{T} \boldsymbol{u}(\ell, t) \otimes \boldsymbol{u}(\ell', t) \mathrm{d}t, \tag{2.4}$$

where $\ell = (r, \theta, z)$ or $\ell = (x, y, z)$ is the position vector in the domain Ω for the pipe or channel geometries, respectively. $\boldsymbol{\Phi}(\ell)$ is the eigenfunction with associated eigenvalue λ, $K(\ell, \ell')$ is the kernel and $\otimes$ denotes an outer product. In order to focus on the turbulent structures, the kernel is built using fluctuating velocities $\boldsymbol{u} = \boldsymbol{U} - \bar{\boldsymbol{U}}$. Mathematically, this makes the basis functions optimal in spanning the fluctuating velocities in L_2. The mean velocity, $\bar{\boldsymbol{U}}$, is found by averaging over all homogeneous directions and time. The temporal integration of the kernel is approximated using a quadrature over a total time period sufficient to sample the turbulent attractor (i.e. $T \approx \infty$). The result of solving this integral equation is that the eigenfunctions $\boldsymbol{\Phi}(\ell)$ form the most optimal basis set, in an $L_2 : (\int_{\Omega} \boldsymbol{u}(\boldsymbol{x}) \cdot \boldsymbol{u}(\boldsymbol{x}) \mathrm{d}\Omega)^{1/2}$ sense, that spans the turbulent flow field data (Holmes *et al.* 1996). The turbulent flow is a superposition of these eigenfunctions (or modes), each with different spatial dependence and dynamics. The eigenfunctions with the largest eigenvalues correspond to the most energetic, largest amplitude dynamics, and much insight is gained by examining the structure and dynamics of these modes.

While very useful, this three-dimensional integral is very computationally intensive to solve, taking more operations to solve than that needed to generate the turbulent flow. To overcome this, there are two techniques used to reduce the size of the computation. The first technique uses the knowledge of the translational invariance of the system and represents the velocities as a Fourier series in the homogeneous directions. For example, with a pipe with two periodic directions (streamwise and azimuthal), the orthogonality of the Fourier series allows the reduction in the three-dimensional integral into multiple one-dimensional integrals, as can be seen in §2*b*(i). The second technique recasts equation (2.3) to a temporal correlation, as long as the total number of eigenfunctions needed to describe the system is much less than the total number of recorded time intervals. While both methods improve the computational tractability of solving the Fredholm integral (equation (2.3)), it will be shown that the most appropriate choice of method depends on the specific goal for which the POD is being used.

(i) *Translational invariance method*

The translational invariance method is a good choice for both the pipe and channel geometries since there are two homogeneous directions. For the channel, they are the streamwise and spanwise directions, and for the pipe the streamwise and azimuthal directions. Owing to this translational invariance, flows that are shifted and rotated are also solutions to the Navier–Stokes equations and belong to the subset of phase space of the turbulent flow. When all of those flows are included in the kernel, the kernel in the homogeneous directions is only a function of the distance between ℓ and ℓ'. Therefore, in polar–cylindrical coordinates, the kernel can be rewritten as

$$K(r, \theta, z, r', \theta', z') = K(r, r', \theta - \theta', z - z')$$
$$= \sum_{n,m}^{\infty} \mathcal{K}(m, n; r, r') \exp(\mathrm{i}n(\theta - \theta')) \exp(\mathrm{i}2\pi m(z - z')/L), \quad (2.5)$$

with azimuthal and streamwise wavenumbers n and m, respectively. The remaining equation with kernel $\mathcal{K}(m, n; r, r')$ is only a one-dimensional integral in the radial direction. Holmes *et al.* (1996) show that the KL eigenfunction dependence in the streamwise and spanwise directions is simply the Fourier series

$$\boldsymbol{\Phi}(r, \theta, z) = \boldsymbol{\Psi}(m, n; r)\mathrm{e}^{\mathrm{i}n\theta} \exp(\mathrm{i}2\pi mz/L). \quad (2.6)$$

In addition, the two-point correlation in a periodic direction is simply its Fourier transform, so the azimuthal and streamwise contributions to the eigenfunctions are extracted *a priori* by taking the Fourier transform of the velocities $\boldsymbol{u}(r, \theta, z) = \sum_{m,n=0}^{\infty} \hat{\boldsymbol{u}}(m, n; r)\mathrm{e}^{\mathrm{i}n\theta} \exp(\mathrm{i}2\pi mz/L)$ and forming the remaining kernel $\mathcal{K}(m, n; r, r')$ for each wavenumber pair n and m. The resulting one-dimensional Fredholm integral is much more computationally tractable:

$$\int_0^R \mathcal{K}(m, n; r, r')\boldsymbol{\Psi}(r')r' \, \mathrm{d}r' = \lambda_{mn}\boldsymbol{\Psi}(m, n; r), \quad (2.7)$$

$$\mathcal{K}(m, n; r, r') = \lim_{T \to \infty} \frac{1}{T} \int_0^T \hat{\boldsymbol{u}}(m, n; r, t) \otimes \hat{\boldsymbol{u}}^{\star}(m, n; r', t) \mathrm{d}t. \quad (2.8)$$

The $\star$ denotes the complex conjugate, and the weighting function r' is present because the integral is evaluated in polar–cylindrical coordinates. Each eigenfunction $\boldsymbol{\Psi}$ now requires three numbers to describe it, $\boldsymbol{k} = (m, n, q)$, with q being the quantum number where the eigenvalue $\lambda_{mnq} > \lambda_{mn(q+1)}$. Since the kernel is built with velocities, it has units of energy; therefore, the terms 'eigenvalue' and 'energy' will be used interchangeably.

(ii) *Method of snapshots*

The second method first proposed by Sirovich (1987), the method of snapshots, recasts the eigenfunction in the Fredholm integral in equation (2.3) as a linear combination of snapshots, where a snapshot refers to an instantaneous flow field. Starting with the projection of the eigenfunction onto the flow field

$$c(t) = \int_{\Omega} \boldsymbol{u}(\ell', t)\boldsymbol{\Phi}(\ell')\mathrm{d}\Omega', \quad (2.9)$$

equation (2.3) can be rewritten as

$$\lim_{T \to \infty} \frac{1}{T} \int_0^T \boldsymbol{u}(\boldsymbol{\ell}, t) c(t) \mathrm{d}t = \lambda \boldsymbol{\Phi}(\boldsymbol{\ell}). \tag{2.10}$$

Integrated on both sides with $\boldsymbol{u}(\boldsymbol{\ell}, t')$ over the entire domain

$$\lim_{T \to \infty} \frac{1}{T} \int_0^T c(t) \int_\Omega \boldsymbol{u}(\boldsymbol{\ell}, t') \boldsymbol{u}(\boldsymbol{\ell}, t) \mathrm{d}\Omega \, \mathrm{d}t = \lambda c(t'), \tag{2.11}$$

$$\lim_{T \to \infty} \frac{1}{T} \int_0^T (\boldsymbol{u}(\boldsymbol{\ell}, t'), \boldsymbol{u}(\boldsymbol{\ell}, t)) c(t) \mathrm{d}t = \lambda c(t'), \tag{2.12}$$

yields a one-dimensional (time) Fredholm integral equation for $c(t)$, where (,) denotes an inner product. This transformation is useful in fluid dynamics since there are typically less time observations (snapshots) than spatial observations (grid points). As before, the integral is intentionally left with the limit as $T \to \infty$. The method of snapshots has an additional constraint on T, in that there must be far greater statistically independent time samples than the number of eigenfunctions needed to describe the system in order to preserve the optimality of the basis set.

It must be noted that one could include in the method of snapshots all of the translationally invariant flow fields (shift and rotate), and the results would equal that of the Fourier method. This is not useful, since the size of the kernel matrix would be $N_x N_z N_s \times N_x N_z N_s$, where N_s is the number of snapshots and N_x and N_z are the number of grid points in the homogeneous directions, respectively. This matrix size is larger than the original kernel as $N_s > N_y$ with N_y being the number of quadrature points in the wall-normal direction.

3. Structures: translational invariance versus method of snapshots

The translational invariance (or Fourier) and snapshot methods each has its benefits and drawbacks. The advantage of the Fourier method is that by its nature many more possible flow fields that are translational invariants of the simulated flow fields are accounted for. Thus, the total simulation time needed for T to approximate infinity in equation (2.4) is less. The downside is that for a given dataset (finite time), the Fourier method does not yield the most optimal basis set, as by its construction it included flow fields that were not a part of the simulation (all of the translational invariants). Conversely, the method of snapshots does yield the most optimal basis set for finite time, yet because the translational invariance is not built in, the simulation must be run for a much longer simulation time for T to approximate ∞. However, at $T = \infty$, the method of snapshots will finally have learned about the translational invariance (i.e. experienced every possible flow field) and so the two methods only agree at $T = \infty$. This was shown by Duggleby & Paul (2008) to be true for a smaller dimensional system, Rayleigh–Bénard convection in a cylindrical domain with aspect ratios 6, 10, 12 and 15.

Figure 1 gives an example mode for the Fourier POD from the turbulent pipe data, the (3, 2, 1) mode and the most energetic mode from the snapshot POD. The figure shows cross-sectional contours of coherent vorticity (or degree of swirl)
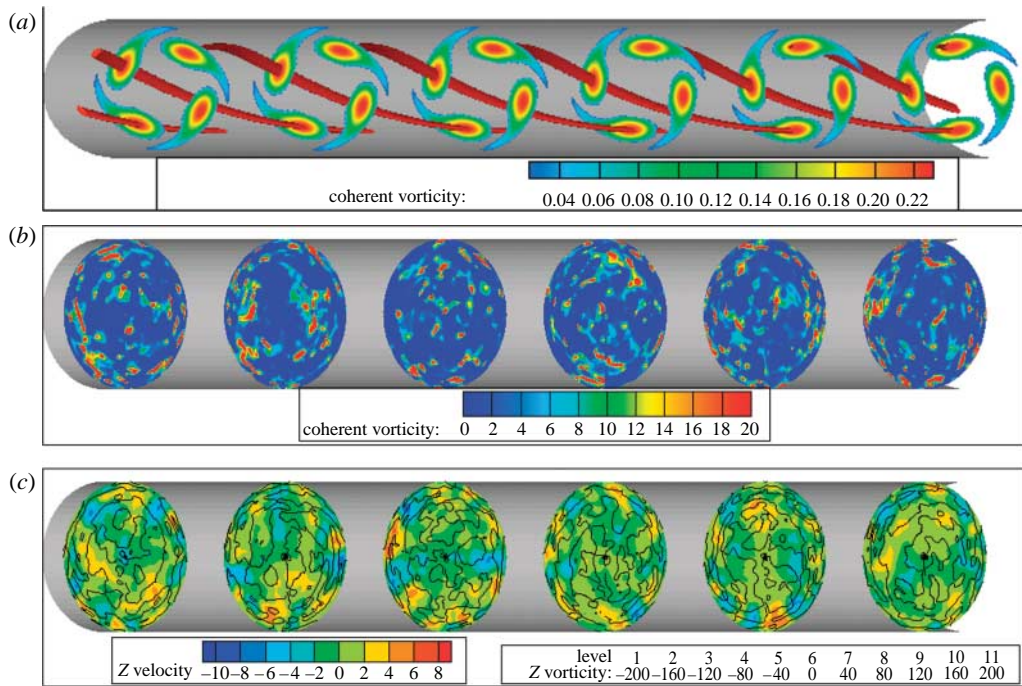
Figure 1. Three-dimensional view of an example (*a*) Fourier POD mode and (*b,c*) a method of snapshots POD mode. The Fourier POD mode is the $(3, 2, 1)$ mode, and plotted are six cross sections of coherent vorticity (degree of swirl) and isosurfaces of 95% maximum coherent vorticity. With a streamwise wavenumber of 3, there are three twists of the structure in the streamwise direction. In a similar fashion, cross sections of (*b*) coherent vorticity and (*c*) streamwise velocity with contours of streamwise vorticity are shown for the most energetic snapshots mode, showing much more spatial variation in its structure in the streamwise and azimuthal directions compared with the Fourier mode.

defined by Chong *et al.* (1990) as imaginary eigenvalues of the strain rate tensor. The snapshot POD mode has more spatial structure, but as $t \to \infty$ it will look more similar to the Fourier POD mode. Figure 2 shows how the two methods predict the dimension of the chaotic attractor. The dimension is approximated by the Karhunen–Loève dimension D_{KL}, the number of modes necessary to capture 90 per cent of the energy of the flow. Because the POD requires an infinite time average (equation (2.4)), the D_{KL} is calculated at multiple intermediate time steps (every 100 snapshots) and then $D_{KL}(T \to \infty) = D_\infty$ is approximated using a curve fit. The Fourier POD quickly settles on an answer because the built-in translational invariance includes more flow fields with finite simulation time, but this comes at the expense of being noisy, as shown in figure 3*a*. The fluctuations in the dimension and the mean flow are closely related. As more energy is distributed among the propagating modes (higher D_{KL}), there is more Reynolds stress production, which slows down the mean flow rate. Therefore, the Fourier method's D_{KL} and mean flow rate have an inverse relationship, as shown in figure 3. Additionally, this noisy nature of the Fourier method's D_{KL} led to the slight underprediction of the dimension $D_{KL} = 2763$ in Duggleby *et al.* (2007*b*), whereas after time averaging, the dimension is predicted to be 4196 with a standard deviation of 584. Conversely,
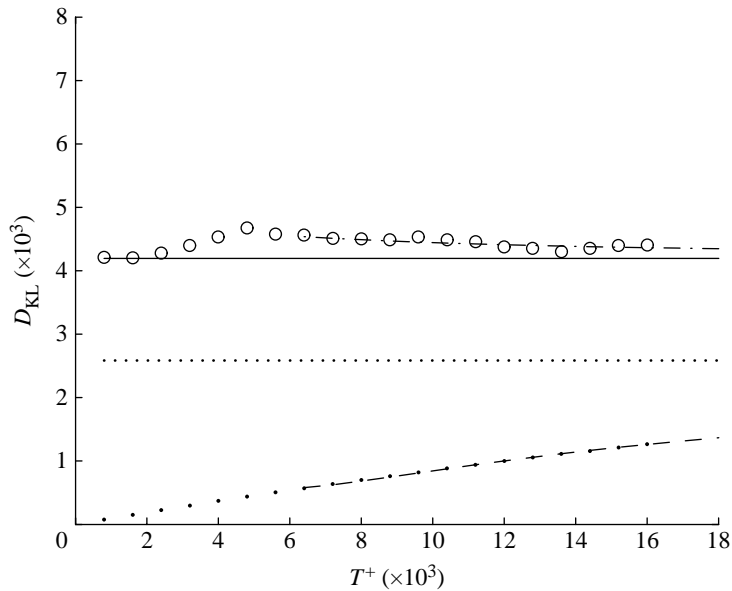
Figure 2. The Karhunen–Loève dimension (D_{KL}) for the Fourier POD with a running average (circles) and the snapshots POD (dots) versus the total time T over which the two-point correlation kernel is averaged. A curve fit (dot-dashed line, Fourier curve fit; dashed line, snapshot curve fit) predicts what D_{KL} would be as $T \to \infty$ (D_{∞}). The Fourier method converges to its predicted D_{∞} (4196 ± 584, solid line) faster, whereas the method of snapshots is slow and after $T^{+} = 16\,800$ yields only a poor prediction ($D_{\infty} = 2584$, dotted line). Conversely, the method of snapshots has a lower dimension at finite time, as it forms a more optimal basis for finite time.
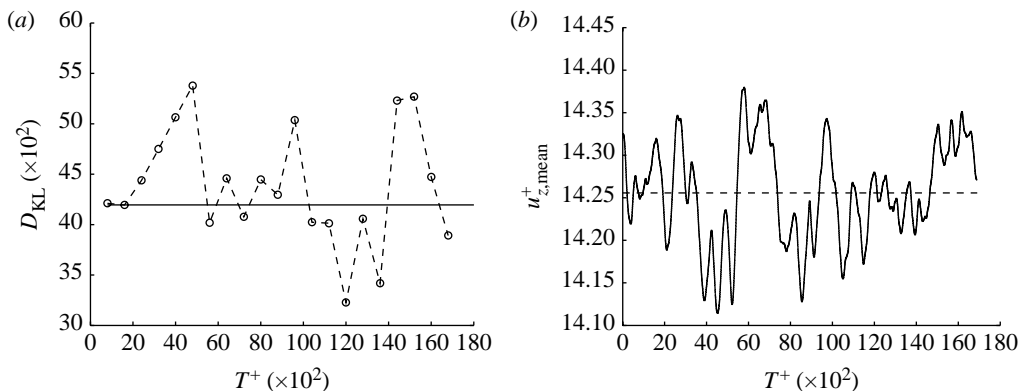

Figure 3. (a) The Karhunen–Loève dimension versus time for the Fourier method (circles) and the predicted D_{∞} (solid line). (b) The mean flow rate versus time (solid curve) and the average mean flow rate (dashed line). D_{KL} versus T shows large variations at different times depending on the total time T over which the kernel in equation (2.4) is averaged. More energy in the propagating modes means a larger dimension and more Reynolds stress production, which slows down the mean flow rate, as can be seen from the inverse relationship between mean flow rate and time (solid curve) and the Fourier dimension (circles).

the snapshot POD is slow to learn about the size of the attractor, and after $T^+ = 16\,800$ only predicts $D_\infty = 2584$, far below the Fourier prediction. At its current predicted rate, D_{KL} for the method of snapshots will be $0.9D_\infty$ when $T = 850\,000\nu/U_t au^2 = 40\,000D/U_{\mathrm{m}}$. At $T = \infty$, the dimensions (and the modes) of both methods will match.

4. Structures and dynamics: pipe versus channel

As discussed in §3, the primary method of choice for POD has been using the translational invariance (Fourier) method to overcome limitations in computational power and memory, making POD accessible. Ever since becoming available, the Fourier POD has successfully extracted flow structures and dynamics of turbulent channel flows. Only recently has POD been extended to turbulent pipe flow (Duggleby *et al.* 2007*b*), and in this section the differences between pipe and channel POD are presented.

(*a*) *Turbulent channel flow*

Numerical simulations were carried out for Reynolds numbers of $Re_\tau = 80$ and 125 (see Sirovich *et al.* 1990, 1991; Ball *et al.* 1991). A general classification of eigenfunctions and associated flow fields was obtained, yielding a fundamental understanding of turbulent flow mechanisms such as bursts and sweeps. For the purpose of outlining those flow characteristics, the $Re_\tau = 80$ data are considered in the following.

Since the flow field was *a priori* expanded in the Fourier series in the periodic streamwise and spanwise directions, the spatial structure of the flow field represented by an eigenfunction with non-zero wavenumbers is that of a sinusoidal wave in these directions. Spatially, this results in a structure similar to an elongated vortex. The wavenumber vector (m, n) determines the angle of the vortex rotation axis in the horizontal plane with respect to the mean flow and also determines the number of waves contained in the respective direction. Sample modes from the FV data are shown in figure 4. It should be noted that even though the integral results of both simulations are in rough agreement (mean flow, root mean square profiles), the two flow fields are slightly different in terms of POD modes, as shown in the list of their respective 25 most energetic modes in table 1. This difference could be attributed to the more dissipative FV approach; however, the data are considered valid to visualize flow structures and mode classification in a qualitative manner.

The mode $\boldsymbol{k} = (0, 2, 1)$ is representative of a subclass of roll modes with $\boldsymbol{k} = (0, n, q)$, as shown in figure 4. These are also the most energetic modes overall, accounting for approximately 45 per cent of the total flow energy. Since they do not propagate in the flow direction, they are termed kinematically degenerate. Their roll structure provides the mechanism of fluid transport from or towards the walls. Together with the propagating waves as described below, they allow for turbulent bursts or sweeps. Thus, they can be deemed responsible for the existence of high- and low-speed streaks in the boundary layer. Some care must be taken when estimating the overall importance of these roll modes since they also contain energy from structures with a slightly off streamwise axis, which could not be accounted for due to the finite grid. The most energetic mode
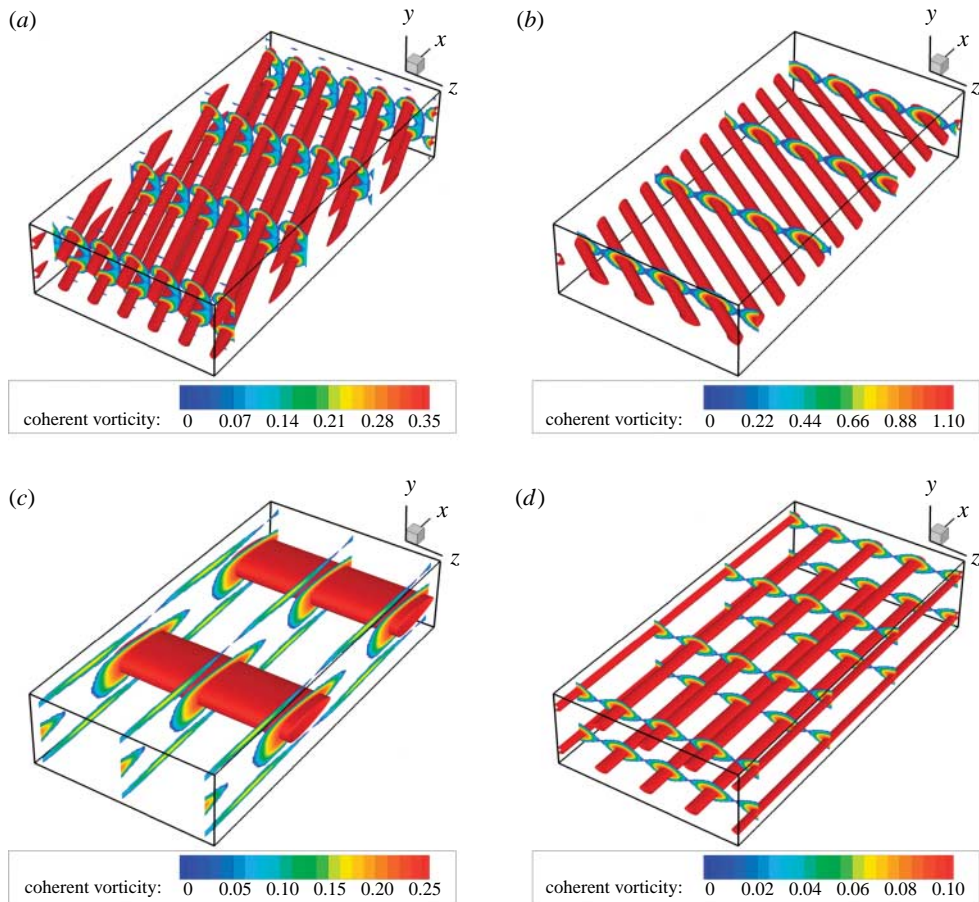
Figure 4. Sample modes from a turbulent channel. (*a*) $(2, 3, 1)$, (*b*) $(6, 2, 1)$, (*c*) $(1, 0, 2)$ and (*d*) $(0, 2, 1)$, showing coherent vorticity.

with both non-zero streamwise and spanwise wavenumbers is $\boldsymbol{k} = (1, 3, 1)$; its wall-normal structure is depicted by the $(2, 3, 1)$ mode in figure 4*a,b* owing to the twice longer domain used for visualization. All modes of this propagating wave class show a nearly constant phase speed, resulting in a travelling wave. The normal speed locus (as a plot of phase speed over wavenumber vector) of the most important members of this class shows that the waves travel with the same speed as the mean flow at a wall-normal location where the Reynolds shear stress is maximal ($y^+ \approx 15$). The eigenfunctions themselves also peak at that location.

Eigenfunctions with both wavenumbers equalling zero do not propagate in any direction and drive the temporal variation of the mean flow. In the wall region, they modify the mean velocity gradient, and in a flow field reconstruction, they appear as shearing modes. The final exception to roll structures occurs for modes with $m > 0$ and $n = 0$. Those modes are aligned in the spanwise direction and can only extract energy from the mean flow. Hence, they are termed parasitic.

Table 1. First 15 eigenvalues ranked in descending order of energy as a percentage of the total energy in the flow (sum of all eigenvalues) for $Re_\tau=80$ and $Re_\tau=125$ channel flow from Sirovich *et al.* (1991), the FV reconstruction of the $Re_\tau=80$ channel and the $Re_\tau=150$ pipe flow from Duggleby *et al.* (2007b). (The mode $\mathbf{k}=(m,n,q)$ has streamwise wavenumber m, spanwise (or azimuthal) wavenumber n and quantum number q such that the eigenvalue (energy) $\lambda_{(m,\,n,\,q)}>\lambda_{(m,\,n,\,q+1)}$.)

	channel $Re_\tau=80$		FV $Re_\tau=80$		channel $Re_\tau=125$		pipe $Re_\tau=150$	
	(m, n, q)	energy (%)	(m, n, q)	energy (%)	(m, n, q)	energy (%)	(m, n, q)	energy (%)
1	(0, 1, 1)	13.00	(0, 3, 1)	6.65	(0, 3, 1)	4.28	(1, 5, 1)	1.62
2	(0, 2, 1)	8.74	(0, 0, 1)	6.08	(0, 1, 1)	3.99	(1, 6, 1)	1.58
3	(0, 3, 1)	7.32	(0, 1, 1)	5.65	(0, 4, 1)	3.27	(1, 3, 1)	1.56
4	(0, 2, 2)	6.93	(0, 2, 1)	5.13	(0, 5, 1)	2.87	(1, 4, 1)	1.42
5	(0, 1, 2)	4.23	(0, 3, 2)	3.67	(0, 4, 2)	2.29	(0, 6, 1)	1.39
6	(0, 3, 2)	4.08	(0, 2, 2)	3.52	(0, 1, 2)	2.20	(1, 7, 1)	1.32
7	(1, 3, 1)	3.27	(0, 4, 1)	3.23	(0, 3, 2)	2.06	(0, 5, 1)	1.28
8	(0, 0, 1)	3.05	(0, 4, 2)	3.13	(0, 2, 1)	1.97	(0, 3, 1)	1.25
9	(1, 3, 2)	2.66	(0, 1, 2)	2.28	(0, 2, 2)	1.88	(1, 2, 1)	1.18
10	(0, 1, 3)	1.88	(1, 3, 1)	1.70	(0, 6, 1)	1.38	(0, 4, 1)	1.11
11	(1, 2, 1)	1.56	(1, 3, 2)	1.50	(0, 5, 2)	1.31	(0, 2, 1)	1.09
12	(0, 0, 2)	1.47	(0, 5, 1)	1.43	(1, 3, 1)	1.25	(2, 4, 1)	1.07
13	(1, 2, 2)	1.37	(1, 4, 1)	1.31	(1, 2, 1)	0.95	(2, 5, 1)	1.00
14	(0, 1, 4)	1.21	(1, 4, 2)	1.28	(1, 4, 1)	0.84	(1, 1, 1)	0.98
15	(0, 2, 3)	1.20	(1, 1, 1)	1.28	(1, 5, 1)	0.83	(2, 7, 1)	0.90

(*b*) *Turbulent pipe flow*

A similar analysis was performed on a turbulent pipe flow simulation with a higher Reynolds number of $Re_\tau=150$ by Duggleby *et al.* (2007b). The modes are qualitatively similar to those found in the channel flow with some slight, but important, differences. Owing to the large difference between $Re_\tau=80$ for the channel and $Re_\tau=150$ for the pipe, the comparison must only be qualitative, but still results in valuable insight.

The first noticeable difference is that $D_{KL}\simeq 4200\pm 600$ for the pipe with $Re_\tau=150$, whereas the channel flow already has $D_{KL}\simeq 4000$ at a lower $Re_\tau=125$. The second, but related, difference is the more uniform distribution of energy for the pipe, as shown in table 1. These differences are most likely due to the channel flow being more unstable than a pipe. For instance, the channel is unstable to infinitesimal disturbances where the pipe requires finite amplitude disturbances to trip the flow. Furthermore, we have observed that a turbulent pipe flow relaminarizes around $Re_\tau=95$, whereas the channel does not relaminarize until $Re_\tau=40$. Therefore, this trend of the pipe geometry suppressing some modes that otherwise would still exist in the channel must carry on well into the turbulent regime. More work is needed in this area to further characterize the physics behind these observations.

By examining the phase speed of the time-dependent coefficients, eigenfunctions can be divided into non-propagating ($m=0$) and propagating ($m\neq 0$) modes, where the average phase speed is constant for the latter. The propagating modes, as in the
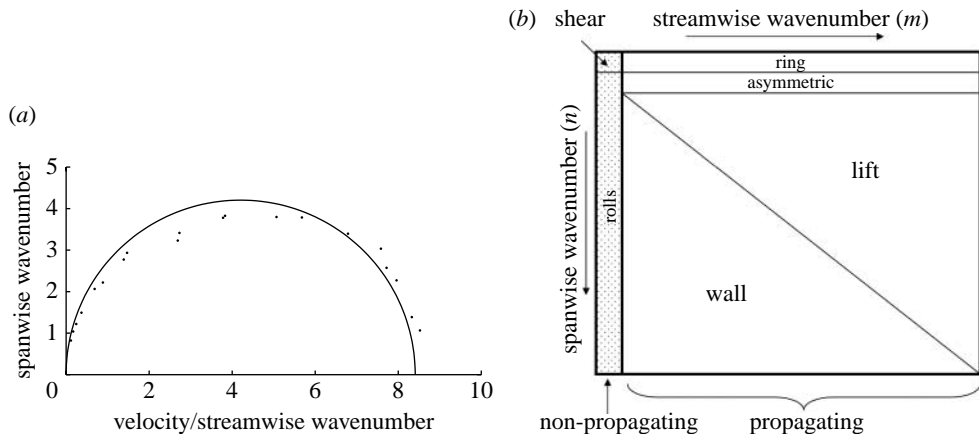
Figure 5. (a) Normal speed locus of top 25 most energetic propagating eigenfunctions for the turbulent pipe flow, normalized with shear velocity u_τ. The circle is a least-squares fit to the data and represents that the wave packets are acting together as a group with a speed of $8.41\,U_\tau$, the point where the circle intersects the y-axis. (b) Subclass classification for turbulent pipe flow according to streamwise (m) and azimuthal (n) wavenumbers.

channel flow, form a wave packet denoted by a nearly circular normal speed locus, as shown in figure 5a. Unlike in channel flow where non-propagating roll structures played the dominant role, the propagating modes are more energetic.

Further subclasses become apparent, for example, by visual inspection of reconstructed flow fields. The subclass classification is shown in figure 5b, and examples of each subclass are shown in figure 6. Within the propagating mode class of the pipe, a higher wavenumber n (azimuthal) than m yields a coherent structure staying close to the wall, termed 'wall mode'. When axial lift is larger than azimuthal turning ($m \geq n$), the structures (or vortices) span from the outer region of the boundary layer to the pipe centre. The angle of the vortex axis in the streamwise–azimuthal plane is determined by the ratio of the corresponding wavenumbers. These modes are an important mechanism of momentum transfer to the pipe centreline, where structures get disrupted by the high-speed main flow. Thus, the higher frequency end of the energy power spectrum (inertial range) is dominantly populated by these lift modes.

Energy transfer between the modes occurs, due to their construction, in a triad interaction due to the nonlinear terms in the Navier–Stokes equations. Webber et al. (2002) showed that with the Fourier POD, these interactions only occur when the wavenumbers (n, m), (n', m') and (n'', m'') add up to zero. Thus, the symmetry-breaking mode (all $n=1$) acts as a catalyst for the energy transfer, which is predominantly from roll (all $n=0$, $m>0$) to wall modes. The energy transfer from wall to lift modes, in turn, is catalysed by the ring modes, which are characterized by the lack of velocity in the azimuthal direction ($n=0$). In a flow field expansion in three dimensions, rings of coherent vorticity become apparent, hence termed 'ring modes'.

In the channel flow, these subclasses do not hold. The main reason is that in a pipe, a given azimuthal wavenumber corresponds to an azimuthal spacing between structures. This spacing is $r\theta$, which is different near the wall than near the centre. Such a wavefront density is only observed near the centre
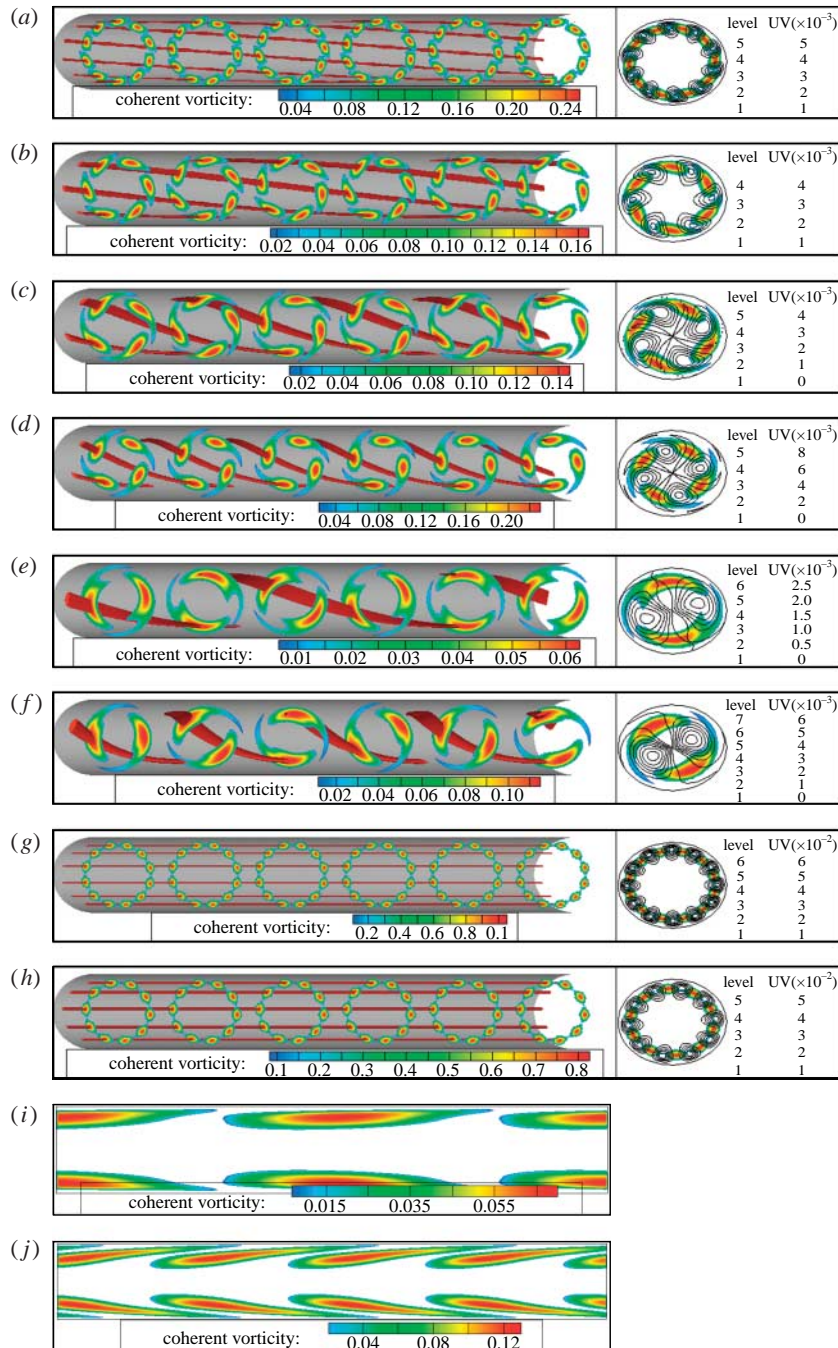
Figure 6. Sample wall modes (*a*) $(1, 5, 1)$ and (*b*) $(1, 3, 1)$, lift modes (*c*) $(2, 2, 1)$ and (*d*) $(3, 2, 1)$, asymmetric modes (*e*) $(1, 1, 1)$ and (*f*) $(2, 1, 1)$, and roll modes (*g*) $(0, 6, 1)$ and (*h*) $(0, 5, 1)$ showing coherent vorticity (left) and a cross section of coherent vorticity with Reynolds stress superimposed (right). The ring modes (*i*) $(1, 0, 1)$ and (*j*) $(2, 0, 1)$ have no streamwise dependence and so only an azimuthal cross section of coherent vorticity is shown.

(outer region) as the wavefront aligns more downstream, corresponding to the lift modes $m \geq n$. For the channel, a spanwise wavenumber corresponds to a constant spanwise spacing independent of the wall-normal distance.

In the non-propagating class, shear (similar to channel flow, with $m=n=0$) and roll modes ($m=0$, all n) are both similar. These modes serve as an energy capacitance, as energy enters from the imposed pressure gradient and then slowly cascades to the propagating waves. These shear modes interact with roll modes, and the roll modes interact with the propagating modes. There is, however, a slight difference between the roll modes in the turbulent channel and pipe flows with regard to energy content. Their cumulative energy content is much higher in the channel flow (also for $Re_\tau = 125$). This can be explained by their larger stretching in the non-periodic direction. For the channel POD, a representative eigenfunction peaks close to 30 wall units away from the wall. In pipe flow, a similar eigenfunction's peak is much closer to the wall (20 wall units) and it flattens towards the pipe centre; the overall contribution to momentum transfer for pipe flow is thus much more limited to the boundary-layer region.

(c) POD interpretation of turbulence

As shown, the same overall structure and dynamics are found in both turbulent channel and pipe flows, implying a similarity in the results of the POD analysis of turbulence. To summarize the contribution POD of turbulent flows, we offer the following model or POD interpretation of turbulence:

  (i) travelling waves exist in the flow, and they act coherently as a wave packet,
 (ii) travelling waves transfer energy from the streamwise rolls—in real space, this coincides to the bursting process,
(iii) the travelling waves are responsible for the majority of the Reynolds stress in the flow, which is increased as more energy lies within the travelling waves, and
 (iv) the self-sustaining mechanism of turbulence in POD space is

   (a) streamwise rolls transfer energy from the mean flow,
   (b) through the 'bursting' process (interaction), the energy passes to travelling waves,
   (c) the travelling waves dissipate quickly, and only maintain energy by constantly being resupplied through energy transfer from the rolls (bursting),
   (d) the catalyst for this interaction are roll modes ($n=0$), which are akin to T-S waves (have no spanwise dependence), and
   (e) the roll modes themselves are energized through the interaction of travelling waves with themselves.

The value of this interpretation is similar to the value of Fourier analysis of homogeneous isotropic turbulence. One may think of this as the extension of Fourier analysis to flows with one non-periodic direction. As computing resources increase, so too will our ability to analyse higher Reynolds number turbulent pipe flows with POD and with more powerful, yet currently inaccessible dynamical analysis tools.

5. Conclusions

The usefulness of POD in examining DNS of turbulence data is shown through the structures and dynamics that it contains. Using the Fourier method, so far the most common method used, the dimension of the chaotic turbulent attractor was estimated to be $D_\infty = 4196 \pm 584$. After only $t^+ = 16\,800$, the method of snapshots still has not seen enough of the attractor to estimate the dimension, and it is predicted that it will reach 90 per cent of D_∞ when $t^+ = 850\,000$. The variation in the Fourier dimension as a function of time is present because the dimension is a measure of the distribution of energy in the turbulent cascade. More energy in the cascade yields greater Reynolds stress production, which diminishes the mean flow rate, as can be seen from the inverse relationship between dimension and mean flow rate. The Fourier dimension also yields smoother structures spatially, and allows for distinctive subclasses based upon wavenumber pairs. Another consequence of the Fourier representation is that the modes with non-zero azimuthal wavenumber propagate with a nearly constant phase speed, they act together as a wave packet, and intermodal energy transfer occurs as a triad interaction. With pipe geometry specifically, the Fourier method also results in a further subclassification beyond that of just propagating and non-propagating modes, yielding different qualitative features for different wavenumber pair regimes (wall modes, lift modes, ring modes, asymmetric modes). The modes found in turbulent channel flow are similar, but without this secondary subclassification. Additionally, an observed difference between turbulent channel and pipe flows is that the dimension of the turbulent chaotic attractor is larger.

In summary, POD provides a powerful means for investigating the complex structures and dynamics found in turbulent pipe flow, and has observed commonality with other wall-bounded flows. This provides the groundwork for a common interpretation of turbulence from a POD point of view. Care must be taken, however, as the POD modes are very dependent on the method chosen and the length of time history of the data. Using these modes in a low-order reconstruction is useful for qualitative observations and quantitative chaos metrics. However, it is challenging to use the POD modes in a predictive capacity as its optimality for future time is not guaranteed. As shown in this paper, further investigations into the chaotic attractor using POD-based metrics may yet uncover a different and useful understanding of turbulence based on nonlinear dynamics and chaos theory.

References

Ball, K. S., Sirovich, L. & Keefe, L. R. 1991 Dynamical eigenfunction decomposition of turbulent channel flow. *Int. J. Numer. Methods Fluids* **12**, 587. (doi:10.1002/fld.1650120606)

Blackwelder, R. F. & Eckelmann, H. 1979 Streamwise vortices associated with the bursting phenomenon. *J. Fluid Mech.* **94**, 577–594. (doi:10.1017/S0022112079001191)

Chong, M. S., Perry, A. E. & Cantwell, B. J. 1990 A general classification of three-dimensional flow fields. *Phys. Fluids A* **2**, 765–777. (doi:10.1063/1.857730)

Duggleby, A. & Paul, M. R. 2008 Exploring extensive chaos in Rayleigh–Bénard convection using fractal and Karhunen–Loève dimensions. In *XXII Int. Conf. Theoretical and Applied Mechanics.*

Duggleby, A., Ball, K. S. & Paul, M. R. 2007*a* The effect of spanwise wall oscillation on turbulent pipe flow structures resulting in drag reduction. *Phys. Fluids* **19**, 125 107. (doi:10.1063/1.2825428)

Duggleby, A., Ball, K. S., Paul, M. R. & Fischer, P. F. 2007*b* Dynamical eigenfunction decomposition of turbulent pipe flow. *J. Turbulence* **8**, 1–28. (doi:10.1080/14685240701376316)

Fischer, P. F., Ho, L. W., Karniadakis, G. E., Ronouist, E. M. & Patera, A. T. 1988 Recent advances in parallel spectral element simulation of unsteady incompressible flows. *Comput. Struct.* **30**, 217–231. (doi:10.1016/0045-7949(88)90228-3)

Green, M. A., Rowley, C. W. & Haller, G. 2007 Detection of Lagrangian coherent structures in three-dimensional turbulence. *J. Fluid Mech.* **572**, 111–120. (doi:10.1017/S0022112006003648)

Holmes, P., Lumley, J. L. & Berkooz, G. 1996 *Turbulence, coherent structures, dynamical systems, and symmetry.* Cambridge, UK: Cambridge University Press.

Keller, L. V. & Friedmann, A. A. 1925 Differentialgleichung für die turbulente bewegung einer kompressiblen flüssigkeit. In *Proc. 1st Int. Congress Applied Mechanics, Delft*, pp. 395–405.

Kim, J., Moin, P. & Moser, R. 1987 Turbulent statistics in fully developed channel flow at low Reynolds number. *J. Fluid Mech.* **177**, 133. (doi:10.1017/S0022112087000892)

Kline, S. J., Reynolds, W. C., Schraub, F. A. & Rundstadler, P. W. 1967 The structure of turbulent boundary layers. *J. Fluid Mech.* **30**, 741–773. (doi:10.1017/S0022112067001740)

Kolmogorov, A. N. 1941 Local structure of turbulence in an incompressible fluid at very high Reynolds numbers. *Dokl. Akad. Nauk SSSR* **30**, 29–303.

Lumley, J. L. 1967 *The structure of inhomogeneous turbulent flows.* Moscow, Russia: Nauka.

Prandtl, L. 1925 Bericht über Untersuchungen zur ausgebildeten Turbulenz. *Z. Angew. Math. Mech.* **5**, 136–139.

Reynolds, O. 1883 An experimental investigation of the circumstances which determine whether the motion of water shall be direct or sinuous, and the law of resistance in parallel channels. *Phil. Trans. R. Soc.* **174**, 935–982. (doi:10.1098/rstl.1883.0029)

Robinson, S. K. 1991 Coherent motions in the turbulent boundary layer. *Annu. Rev. Fluid Mech.* **23**, 601–639. (doi:10.1146/annurev.fl.23.010191.003125)

Sirovich, L. 1987 Turbulence and the dynamics of coherent structures. Part I: coherent structures. *Q. Appl. Math.* **XLV**, 561–571.

Sirovich, L., Ball, K. S. & Keefe, L. R. 1990 Plane waves and structures in turbulent channel flow. *Phys. Fluids A* **12**, 2217–2226. (doi:10.1063/1.857808)

Sirovich, L., Ball, K. S. & Handler, R. A. 1991 Propagating structures in wall-bounded turbulent flows. *Theor. Comput. Fluid Dyn.* **2**, 307. (doi:10.1007/BF00271470)

Taylor, G. I. 1921 Diffusion by continuous movements. *Proc. Lond. Math. Soc.* **20**, 196–211. (doi:10.1112/plms/s2-20.1.196)

Taylor, G. I. 1935 Statistical theory of turbulence, I–III. *Proc. R. Soc. A* **151**, 465–478. (doi:10.1098/rspa.1935.0161)

Townsend, A. A. 1956 *The structure of turbulent shear flows.* Cambridge, UK: Cambridge University Press.

Tufo, H. M. & Fischer, P. F. 1999 Terascale spectral element algorithms and implementations. In *Proc. of the ACM/IEEE SC99 Conf. on High Performance Networking and Computing.* Gordon Bell Prize paper, IEEE Computer Society.

von Kármán, T. 1930 Mechanische Ähnlichkeit und Turbulenz. In *Nachr. Ges. Wiss. Göttingen, Math.-Phys. KL.*, pp. 58–76.

Webber, G. A., Handler, R. A. & Sirovich, L. 2002 Energy dynamics in a turbulent channel flow using the Karhunen–Loève approach. *Int. J. Numer. Methods Fluids* **40**, 1381–1400. (doi:10.1002/fld.414)